Inorg. Chem. **1999,** *38,* 5593−5601

Exchange Interactions Derived from Electron-Transfer Processes in $[Cr_2(OH)_3(tmtame)_2](NO_3)_3$

Ralph Schenker,[†] Høgni Weihe,[‡] and Hans U. Güdel*,[†]

Departement für Chemie und Biochemie, Universität Bern, Freiestrasse 3,
CH-3000 Bern 9, Switzerland, and H. C. Ørsted Institutet, Københavns Universitet,
Universitetsparken 5, DK-2100 København Ø, Denmark

Received April 13, 1999

From polarized optical absorption and emission spectra of $[Cr_2(OH)_3(tmtame)_2](NO_3)_3$ (tmtame = *N,N′,N″*-trimethyl-1,1,1-tris(aminomethyl)ethane) in the visible and near UV, the exchange splittings of the $^4A_2{}^4A_2$ ground as well as the $^2E^4A_2$ and $^2T_1{}^4A_2$ singly and $^2E^2E$, $^2E^2T_1$, $^2T_1{}^2T_1$, $^2E^2T_2$, and $^2T_1{}^2T_2$ doubly excited states of the ground electron configuration are determined, the latter corresponding to simultaneous pair excitations by a single photon. The bulk of intensity in the region of these doubly excited states is found to be vibronically induced by an electric-dipole exchange mechanism. From single-crystal and glass absorption spectra a ferromagnetic energy ordering of the lowest energy ligand-to-metal charge transfer (LMCT) states is derived, whereas the ground state is antiferromagnetically split. The observed splittings are rationalized using a model based on a valence bond approach (VBCI), where the exchange interactions are derived from configuration interaction of LMCT and metal-to-metal charge transfer (MMCT) electron configurations with the ground configuration. The splittings are well reproduced by this model over a range of about 40 000 cm^{-1}. Trigonal orbital exchange parameters J_a and J_e are derived, revealing that the direct pathway along the Cr−Cr axis is the dominant one. This gives rise to a double exchange situation in the LMCT configuration, leading to the observed ferromagnetic energy ordering of LMCT levels. Magnetostructural correlations are established from a comparison of the title compound with the similar complex $[Cr_2(OH)_3(tmtacn)_2](ClO_4)_3$ (tmtacn = 1,4,7-trimethyl-1,4,7-triazacyclononane).

1. Introduction

Current attempts to synthesize new magnetic materials based on transition metal ions have given the study of exchange interactions in magnetic clusters a renaissance. In extended lattices interactions between nearest neighbors are the dominant ones. Transition metal dimers are thus ideal candidates for the study of these interactions. Exchange splittings of ground and excited states in a great number of such complexes containing paramagnetic ions were investigated using optical spectroscopic techniques.[1] Spin-forbidden excitations within the ground electron configuration such as $^4A_2 \rightarrow {}^2E$ and $^4A_2 \rightarrow {}^2T_1$ in Cr^{3+} are of particular interest, since they often consist of sharp lines and can thus be very informative. In a dimer these excited states are written as $^2E^4A_2$ and $^2T_1{}^4A_2$, and they are called singly excited (SE) states, since formally only one of the two centers is excited. The exchange splittings of the $^4A_2{}^4A_2$ ground and the $^2E^4A_2$ and $^2T_1{}^4A_2$ SE states were investigated in great detail for a number of mono-,[2] di-,[3−6] and tri-*μ*-hydroxo[7,8] bridged chromium(III) dimers. The observed energy splittings in the ground and SE states were modeled separately, using exchange parameters as model parameters. The exchange parameters derived from the SE state splittings were found to be about 25−100% larger than for the ground state,[3,5,7,8] indicating an increase of the exchange interactions with increasing energy. This behavior was found to be typical for exchange-coupled systems,[1] but so far it has not been reproduced by a theoretical model.

Exchange interactions are intimately related to electron-transfer processes. In early work the kinetic exchange was formally derived from a metal-to-metal (MM) electron-transfer configuration at energy *U*.[9] Recently the ligand-to-metal (LM) electron-transfer configurations were explicitly included by Solomon, Tuczek, and co-workers,[10] focusing on the LM charge transfer (LMCT) configuration in various dinuclear Cu^{2+} [11,12] and Fe^{3+} [13] complexes. The observed substantial exchange splittings in this configuration were rationalized using a valence bond approach (valence bond configuration interaction model, VBCI). So far this treatment has only been used for the interpretation of ground and LMCT state splittings. In the title compound we have been able to account for the observed lowest energy LMCT bands using a VBCI approach.[14]

---

* Author for correspondence. E-mail: hans-ulrich.guedel@iac.unibe.ch.
[†] Universität Bern.
[‡] Københavns Universitet.

(1) McCarthy, P. J.; Güdel, H. U. *Coord. Chem. Rev.* **1988**, *88*, 69.
(2) Riesen, H.; Güdel, H. U. *Inorg. Chem.* **1986**, *25*, 3566.
(3) Schönherr, T. *J. Mol. Struct (THEOCHEM)* **1992**, *261*, 203.
(4) Decurtins, S.; Güdel, H. U.; Pfeuti, A. *Inorg. Chem.* **1982**, *21*, 1101.
(5) Decurtins, S.; Güdel, H. U. *Inorg. Chem.* **1982**, *21*, 3598.
(6) Reber, C.; Güdel, H. U.; Spiccia, L.; Marty, W. *Inorg. Chem.* **1987**, *26*, 3186.
(7) Riesen, H.; Güdel, H. U. *Mol. Physics* **1987**, *60*, 1221.
(8) Riesen, H.; Reber, C.; Güdel, H. U.; Wieghardt, K. *Inorg. Chem.* **1987**, *26*, 2747.
(9) Anderson, P. W. *Phys. Rev.* **1959**, *115*, 2.
(10) Tuczek, F. In: *Spectroscopic Methods in Bioinorganic Chemistry*; Solomon, E. I., Hodgson, K. E., Eds.; American Chemical Society: Washington, DC, 1998, Chapter 5.
(11) von Seggern, I.; Tuczek, F.; Bensch, W. *Inorg. Chem.* **1995**, *34*, 5530.
(12) Tuczek, F.; Solomon, E. I. *Inorg. Chem.* **1993**, *32*, 2850.
(13) Brown, C. A.; Remar, G. J.; Musselman, R. L.; Solomon, E. I. *Inorg. Chem.* **1995**, *34*, 688.
(14) Schenker, R.; Weihe, H.; Güdel, H. U. *Chem. Phys. Lett.* **1999**, *303*, 229.

10.1021/ic9904081 CCC: $18.00

Scheme 1

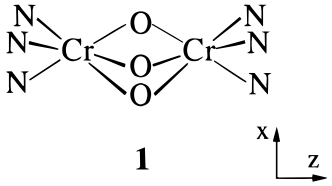

1

We measured polarized optical absorption and luminescence spectra in the visible and near UV of the tri-μ-hydroxo bridged Cr^{3+} dimer $[Cr_2(OH)_3(tmtame)_2](NO_3)_3$ **1**, where tmtame is *N*,*N′*,*N″*-trimethyl-1,1,1-tris(aminomethyl)ethane. The spectra are similar to those of $[Cr_2(OH)_3(tmtacn)_2](ClO_4)_3$ (tmtacn = 1,4,7-trimethyl-1,4,7-triazacyclononane) **2** reported in ref 7, and the observed exchange splittings of the $^2E^4A_2$ and $^2T_1{}^4A_2$ singly excited states are thus analyzed in comparison. In the near UV the absorption spectra show highly structured sharp and prominent bands at approximately the sum of the energies of two single excitations. These so-called double excitations (DE), corresponding to the simultaneous excitation of both ions by a single photon, were also observed in **2**,[7] but no interpretation was offered at that time.

We adapted the VBCI model used in ref 10 to our specific situation in **1**. This allows us to model the observed energy splittings in the ground, SE, and DE states of the ground configuration as well as those of the lowest energy LMCT configurations with only one parameter set. This is in contrast to previous treatments, in which one parameter set was used for the description of the ground state splitting and another one for the splitting of the SE states, whereas the DE states were most often not taken into account. From the model parameters orbital exchange parameters are derived, revealing the relative importance of the different exchange pathways. The differences in the energy splittings of complexes **1** and **2** are ascribed to structural differences.

2. Experimental Section

2.1. Synthesis and Crystal Growth. All the chemicals used for the present study were of analytical grade. The dinuclear complex $[Cr_2(OH)_3(tmtame)_2]Cl_3{\cdot}4H_2O$ was synthesized as described in ref 15. The nitrate salt $[Cr_2(OH)_3(tmtame)_2](NO_3)_3$ **1** was obtained by addition of 15 g of $LiNO_3$ to 4.00 g of $[Cr_2(OH)_3(tmtame)_2]Cl_3{\cdot}4H_2O$ dissolved in 30 mL of water at 50 °C. After cooling, the crystalline powder was filtered off and washed with a saturated solution of $LiNO_3$ and ethanol. Yield: 3.24 g.

Anal. Calcd for **1**: Cr, 15.77%; C, 29.14%; H, 6.88%; N, 19.11%. Found: Cr, 15.80%; C, 29.06%; H, 6.83%; N, 19.17%.

Hexagonal prisms up to 0.4 mm in diameter and 0.6 mm in length were grown by evaporating a concentrated aqueous solution of $[Cr_2(OH)_3(tmtame)_2](NO_3)_3$ within 3−5 days at room temperature. The molecular symmetry of the complex is assumed to be C_{3h} with a Cr−Cr distance of 2.636 Å from a comparison with ref 15, and the 3-fold axis was found to lie parallel to the hexagonal crystal axis *c*. Scheme 1 shows the main structural features of the dimeric complex. The orthogonal coordinate system used in the model is shown, with the *y* vector pointing out of the paper plane. The Cr single-ion and dimer symmetries are approximately C_{3v} and D_{3h}, respectively.

2.2. Spectroscopic Measurements. Absorption spectra were measured in the spectral range of 700−210 nm. The hexagonal crystal prisms were ideal for absorption measurements of the weak SE in both σ and π polarizations (electric vector of the light perpendicular and parallel to the *c* axis, respectively) as well as in axial orientation (α, unpolarized light propagating along the *c* axis). For polarized absorption measurements below 580 nm a single crystal was ground to a thin disk containing the *c* axis. We embedded the crystal with correct orientation in molten glycolphthalate at 105 °C. After cooling to room temperature, we carefully polished the crystal until the size of the polished area reached a maximum. Afterward we turned the crystal and polished it from its back. A sample of 250 × 250 × 65 μm^3 was thus obtained. Below 260 nm the optical density was too high for crystal measurements, and the compound was dissolved in a 95/5% glycerol/water solution, which forms a transparent glass on cooling.

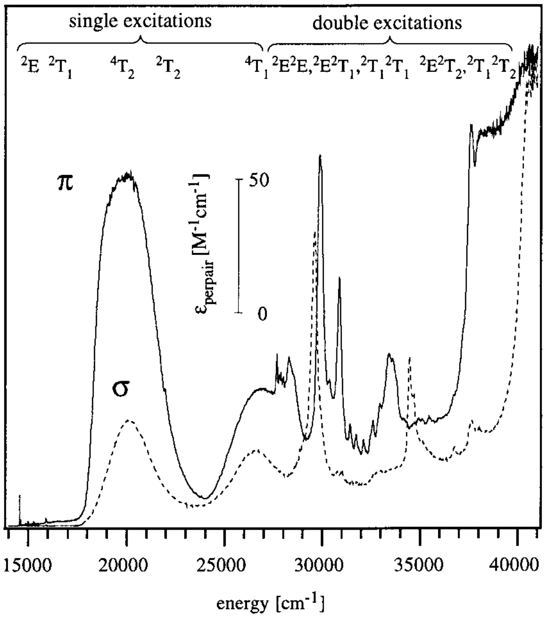

Figure 1. σ and π polarized 10 K absorption spectra in the visible and near UV. The bands are designated in *O* notation.

Absorption spectra in the visible and UV were recorded on a double-beam spectrometer Cary 05e. Variable sample temperatures between 10 and 300 K were achieved using a closed-cycle helium refrigerator (Air Products). Luminescence was dispersed by a 0.85 m double monochromator (Spex 1402) and detected by a cooled PM tube (RCA 31034) in conjunction with a photon counting system (SR 400). An Ar^+ ion laser (Ion Laser Technology 5450A) was used as an excitation source. The sample was cooled to 10 K using a cold helium-gas flow technique.

3. Optical Spectra

The σ and π polarized 10 K absorption spectra in the visible and near UV are shown in Figure 1. The bands are designated in *O* notation. As usually found for binuclear chromium(III) complexes, the $^4T_2$ and $^4T_1$ bands are hardly affected by the exchange interactions, since the splittings are much smaller than the line widths, and the intensities are not much influenced by the coupling. A striking new feature compared to the spectra of mononuclear chromium(III) compounds is the very prominent, sharp lines in the near UV region. The oscillator strengths of the most intense of these DE bands are comparable to those of the spin-allowed bands. The σ spectrum is identical with the α spectrum (not shown), indicating the electric-dipole character of all the transitions. The intensity is generally larger in π than in σ polarization. Transitions to $^2E^4A_2$, $^2T_1{}^4A_2$ and $^2T_2{}^4A_2$ SE states are observed as very weak and sharp features around 15 000 and 21 000 cm^{-1}, respectively; see Figure 1.

The σ and π polarized absorption spectra between 14 000 and 17 000 cm^{-1} are enlarged in Figure 2 for three selected temperatures. The spectra reveal a rich fine structure, and they are strongly temperature dependent between 10 and 295 K. The observed bands arise from $^4A_2{}^4A_2 \rightarrow {}^2E^4A_2$, $^2T_1{}^4A_2$ SE transitions within the t_2 orbitals (in *O* notation). Their oscillator strengths are found to be enhanced by 1−2 orders of magnitude

---

(15) Glerup, J.; Larsen, S.; Weihe, H. *Acta Chem. Scand.* **1993**, *47*, 1154.

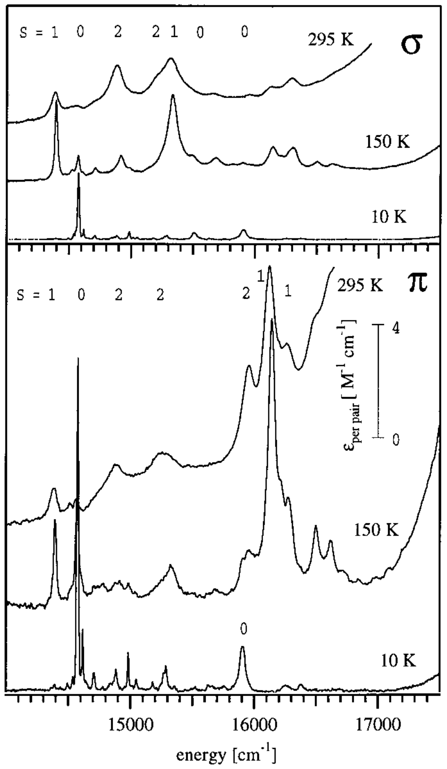

Figure 2. Single-crystal absorption spectra in σ (top graph) and π (bottom graph) polarizations in the region of the $^4A_2{}^4A_2 \rightarrow {}^2E^4A_2$, $^2T_1{}^4A_2$ single excitations at three different temperatures. The S numbers indicate the spin of the initial ground state level.

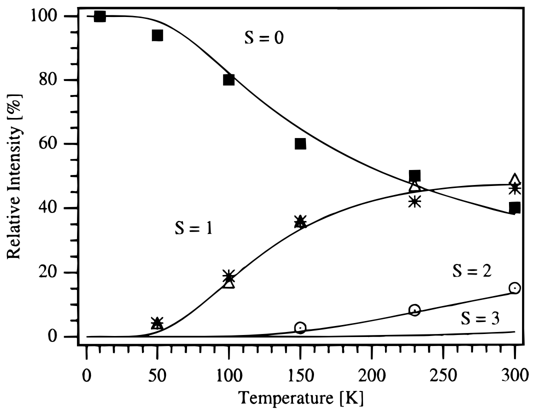

Figure 3. Temperature dependence of the intensity of some $^4A_2{}^4A_2 \rightarrow {}^2E^4A_2$, $^2T_1{}^4A_2$ absorption bands compared to the Boltzmann distribution (solid lines) within the four ground-state spin levels labeled with their spin quantum numbers S. The following transitions were used: Δ, $^3A_2'' \rightarrow {}^3E''$ ($^2E^4A_2$) at 14 392 cm^{-1}; ■, $^1A_1' \rightarrow {}^3E''$ ($^2E^4A_2$) at 14 575 cm^{-1} ⊙, $^5A_1' \rightarrow {}^5E'(^2E^4A_2)$ at 14 915 cm^{-1}; * , $^3A_2'' \rightarrow {}^3A_1'$ ($^2A_2(^2T_1)^4A_2$) at 16 145 cm^{-1}. The intensities are scaled to 100%.

with respect to those of a corresponding mononuclear complex. Three different temperature dependences are recognized, corresponding to the Boltzmann population of the three lowest ground state dimer levels, which are denoted with their spin quantum numbers S in Figure 2. In Figure 3 the temperature dependence of a few selected bands is shown. Table 1 lists the energies and polarizations of all the observed $^2E^4A_2$ and $^2T_1{}^4A_2$ absorptions.

Figure 4 shows the polarized absorption spectra in the near UV at temperatures between 10 and 295 K. A great number of relatively sharp bands are observed, which exhibit differences in intensity of 3 orders of magnitude between the most intense and the weakest lines. All the bands are completely polarized. The overall intensity is considerably larger in π than in σ polarization. The bands observed at 10 K all originate in the S = 0 dimer ground level, whereas the hot intensity arises from

Table 1. Energies (cm^{-1}), Polarizations, Temperatures (K), and Assignment of the Observed Transitions to SE Dimer Levels in the Visible[a]

energy	polarizn	temp	assignment
14 060		10	$^5A_1' \leftarrow {}^3E''(^2E^4A_2)$
14 392	π/σ	50	$^3A_2'' \rightarrow {}^3E''(^2E^4A_2)$
14 432	σ	50	$^3A_2'' \rightarrow {}^3E'(^2E^4A_2)$
14 575	π/σ	10	$^1A_1' \rightarrow {}^3E''(^2E^4A_2)$
14 615	π/σ	10	$^1A_1' \rightarrow {}^3E'(^2E^4A_2)$
14 915	σ	150	$^5A_1' \rightarrow {}^5E'(^2E(^2T_1)^4A_2)$
15 229	σ	230	$^5A_1' \rightarrow {}^5E''(^2E(^2T_1)^4A_2)$
15 336	σ	50	$^3A_2'' \rightarrow {}^3E''(^2E(^2T_1)^4A_2)$
15 516	σ	10	$^1A_1' \rightarrow {}^3E''(^2E(^2T_1)^4A_2)$
15 627	σ	10	$^1A_1' \rightarrow {}^3E'(^2E(^2T_1)^4A_2)$
15 910	π/σ	10	$^1A_1' \rightarrow {}^3A_2''(^2A_2(^2T_1)^4A_2)$
15 955	π/σ	150	$^5A_1' \rightarrow {}^5A_2''(^2A_2(^2T_1)^4A_2)$
16 145	π/σ	50	$^3A_2'' \rightarrow {}^3A_1'(^2A_2(^2T_1)^4A_2)$
20 700	σ	10	$^4A_2{}^4A_2 \rightarrow {}^2T_2{}^4A_2$
21 960	π/σ	10	$^4A_2{}^4A_2 \rightarrow {}^2T_2{}^4A_2$
23 509	π	10	$^4A_2{}^4A_2 \rightarrow {}^2T_2{}^4A_2$
23 807	π	10	$^4A_2{}^4A_2 \rightarrow {}^2T_2{}^4A_2$

[a] The lowest temperature at which a given transition is observed is indicated. The lowest energy transition at 14 060 cm^{-1} is observed in emission.

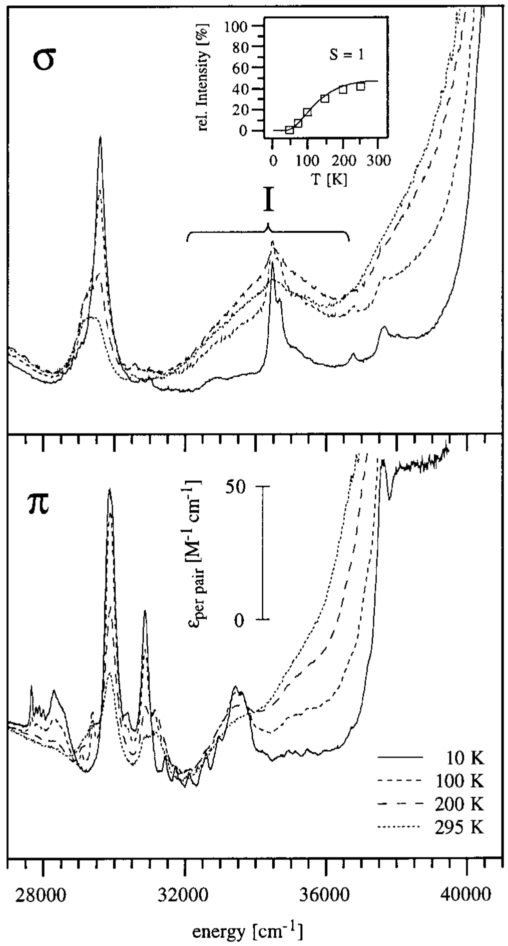

Figure 4. Single-crystal absorption spectra in σ (top graph) and π (bottom graph) polarizations in the region of the $^2E^2E$, $^2E^2T_1$, $^2T_1{}^2T_1$, $^2E^2T_2$, and $^2T_1{}^2T_2$ double excitations at three different temperatures. The inset shows the temperature dependence of intensity of the LMCT band labeled by I (squares) compared to the Boltzmann population of the $^3A_2''$ ground state level (solid line).

Table 2. Energies (cm^{-1}), Polarizations, Oscillator Strengths, Temperature Ranges (K), and Assignment of the Observed Transitions to DE Dimer Levels in the UV Region[a]

energy	polarizn	temp	f	assignment
27 672	π	10	6.5×10^{-6}	
27 801	π	10	3.3×10^{-6}	
27 894	π	10	3.3×10^{-6}	
28 002	π	10	3.3×10^{-6}	
28 139	π	10	3.3×10^{-6}	
28 297	π	10	2.1×10^{-5}	$^1A_1' \rightarrow {}^1A_1' + \nu(a_2'')$
28 308	σ	10	3.3×10^{-7}	
28 477	σ	10	3.3×10^{-7}	
28 549	π	10	5.6×10^{-6}	
28 585	σ	10	1.1×10^{-6}	
28 718	σ	10	1.1×10^{-6}	
28 862	σ	10	2.2×10^{-6}	
28 900	σ	100	1.3×10^{-5}	
28 989	σ	10	2.2×10^{-6}	
29 080	π	50	1.3×10^{-5}	
29 099	σ	10	2.2×10^{-6}	
29 124	σ	75	5.2×10^{-5}	$^3A_2'' \rightarrow {}^3A_2'' + \nu(e')$ $(^2A_2(^2T_1)^2A_2(^2T_1))$
29 400	π	50	5.2×10^{-5}	$^3A_2'' \rightarrow {}^3A_2'' + \nu(a_2'')$ $(^2A_2(^2T_1)^2A_2(^2T_1))$
29 600	σ	10	1.9×10^{-4}	$^1A_1' \rightarrow {}^1A_1' + \nu(e')$ $(^2A_2(^2T_1)^2A_2(^2T_1))$
29 875	π	10	1.9×10^{-4}	$^1A_1' \rightarrow {}^1A_1' + \nu(a_2'')$ $(^2A_2(^2T_1)^2A_2(^2T_1))$
30 375	π	10	2.2×10^{-5}	
30 572	σ	100	5.6×10^{-6}	
30 770	σ	10	1.1×10^{-6}	
30 876	π	10	7.6×10^{-5}	$^1A_1' \rightarrow {}^1A_1' + \nu(a_2'')$
31 005	σ	10	2.2×10^{-6}	
31 130	π	100	5.2×10^{-5}	$^3A_2'' \rightarrow {}^3A_2'' + \nu(a_2'')$
31 430	π	10	3.3×10^{-6}	
31 510	σ	10	3.3×10^{-7}	
31 723	π	10	3.3×10^{-7}	
31 810	σ	10	3.3×10^{-7}	
32 108	π	10	2.8×10^{-6}	
32 480	π	10	3.3×10^{-6}	
32 600	π	10	6.5×10^{-6}	
32 883	σ	10	4.2×10^{-6}	
32 946	π	10	1.3×10^{-5}	
33 422	π	10	4.3×10^{-5}	$^1A_1' \rightarrow {}^1A_1' + \nu(a_2'')$
33 600	π	10	8.6×10^{-6}	
33 822	π	10	1.1×10^{-5}	
34 178	σ	10	2.2×10^{-6}	
34 197	π	10	2.6×10^{-6}	
34 482	σ	10	4.8×10^{-5}	$^1A_1' \rightarrow {}^1A_2' + \nu(e')$ $(^2A_2(^2T_1)^2A_1(^2T_2))$
34 690	σ	10	1.9×10^{-5}	
34 717	π	10	1.3×10^{-6}	
34 943	π	10	1.2×10^{-6}	
35 092	σ	10	8.7×10^{-6}	
35 127	π	10	1.2×10^{-6}	
35 285	σ	10	1.3×10^{-6}	
35 470	π	10	2.2×10^{-6}	
35 496	σ	10	2.2×10^{-6}	
35 900	σ	10	1.1×10^{-6}	
35 950	π	10	2.2×10^{-6}	
36 730	π	10		
36 780	σ	10	3.3×10^{-6}	
37 205	π	10		
37 600	π	10	$>4.1 \times 10^{-5}$	$^1A_1' \rightarrow {}^1A_1' + \nu(a_2'')$
37 660	σ	10	2.1×10^{-5}	
38 400	σ	10	1.1×10^{-6}	

[a] Oscillator strengths are corrected for the appropriate Boltzmann population.

$S = 1$ transitions. A prominent hot band is the σ polarized band centered at about 34000 cm^{-1} and labeled I in Figure 4. Its intensity follows the Boltzmann population for the $S = 1$ ground state level, as shown in the inset. The energies, polarizations, and intensities of the observed DE bands are listed in Table 2.

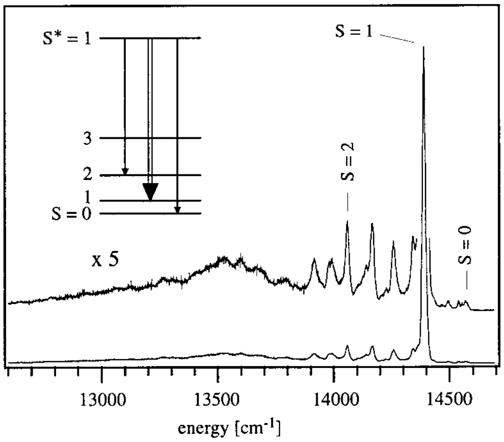

Figure 5. Unpolarized luminescence spectrum at 10 K after excitation at 514.5 nm. The purely electronic transitions are assigned to the ground state spin levels. The inset shows the energy level diagram including the observed electronic transitions to ground state levels.

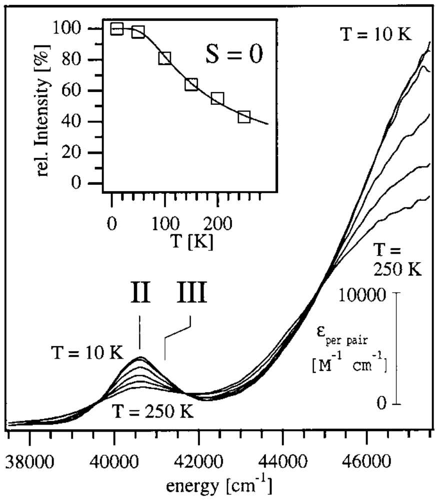

Figure 6. Glycerol glass absorption spectra in the ultraviolet region at various temperatures between 10 and 250 K. II and III denote the $^1A_1' \rightarrow {}^1A_2''$ and $^1A_1 \rightarrow {}^1A_1''$ LMCT transitions, respectively. The inset shows the temperature dependence of intensity of the two bands (squares) compared to the Boltzmann population of the $^1A_1'$ ground state level.

Figure 5 shows the unpolarized luminescence of a single crystal at 10 K after excitation at 19436 cm^{-1}. Together with the absorption spectra (Figure 2) it is the key for the determination of the $^4A_2{}^4A_2$ ground state splitting. Due to its high intensity in emission, the very prominent line at 14 392 cm^{-1} is assigned to a $S^* = 1 \rightarrow S = 1$ transition. From the coincidence of the lines at 14 392 and 14 575 cm^{-1} in absorption and emission, we conclude that the $S = 1$ lies 183 cm^{-1} above the $S = 0$ ground state level. From comparison with the emission spectrum of **2**,[7] the line at 14 060 cm^{-1} is assigned to the $S^* = 1 \rightarrow S = 2$ transition, leading to a $S = 2 - S = 1$ separation of 332 cm^{-1}. The three dimer transitions shown in the inset of Figure 5 are thus observed. They define the antiferromagnetic ground state splitting pattern. The spectrum in Figure 5 is contaminated by some trap emission.

The glycerol glass spectra of the broad bands in the UV between 10 and 250 K are shown in Figure 6. Two cold LMCT bands are observed at 40 600 and 41 200 cm^{-1}, labeled II and III, respectively. They are found to be π polarized from a comparison of the crystal and glass spectra; compare with Figure 4. Their intensity follows the Boltzmann population for the $S = 0$ ground state level, as shown in the inset. There is a very intense broad band centered at about 47000 cm^{-1}. Its intensity is about 50% higher at 10 K than at 250 K. Its polarization cannot be determined.

4. Theory

4.1. Energy Splittings: VBCI Model. We adapt the VBCI model used by Solomon, Tuczek et al.[10] to account for exchange splittings of the ground and LMCT configurations in dinuclear Cu^{2+} complexes to our specific situation in **1**. It uses a valence bond approach and explicitly calculates configuration interactions under the action of a one-electron operator. The matrix elements are treated as model parameters to be determined experimentally.

We take three electron configurations into account (see Figure 7), namely the ground (GR), an LMCT, and a metal-to-metal (MMCT) electron transfer configuration, designated as

$$\begin{gathered}(t_2^3)_A L^N (t_2^3)_B \\ (t_2^4)_A L^{N-1} (t_2^3)_B / (t_2^3)_A L^{N-1} (t_2^4)_B \\ (t_2^2)_A L^N (t_2^4)_B / (t_2^4)_A L^N (t_2^2)_B \qquad (1)\end{gathered}$$

respectively. A and B stand for the two Cr^{3+} centers. L and N symbolize the bridging ligand orbitals and the number of their electrons, respectively. The nature of the L orbitals will be specified below. The metal e orbitals (in O notation) are not included. Δ and U are the energies of the lowest LMCT and MMCT states relative to the ground state, respectively, in the absence of exchange interaction; see Figure 7. The single-ion energies of the octahedral ligand-field states ^2E, $^2T_1$, and $^2T_2$ are represented by the parameters $R(^2E)$, $R(^2T_1)$, and $R(^2T_2)$, respectively. In the approximate C_{3v} site symmetry of the Cr^{3+} ions in **1** (see Scheme 1), the t_2 orbitals are split by δ_{t_2} into two sets of orbitals with a_1 and e symmetry.

According to Scheme 1 two types of interaction are considered: a direct interaction between orbitals centered on the metal centers A and B, often called direct exchange, and an indirect interaction involving ligand orbitals, often called superexchange.[9] A direct interaction between $(a_1)_A$, $(a_1)_B$ or $(e)_A$, $(e)_B$ will result in the following nonzero matrix elements, respectively:

$$h_{\sigma_{MM}} = \langle (a_1)_A | \hat{h} | (a_1)_B \rangle \qquad (2)$$

$$h_{\pi_{MM}} = \langle (e_x)_A | \hat{h} | (e_x)_B \rangle = \langle (e_y)_A | \hat{h} | (e_y)_B \rangle \qquad (3)$$

where e_x and e_y are the two components of the e representation, $\hat{h}$ is a one-electron operator, and the integrals in eqs 2 and 3 are electron-transfer integrals. There exist a multitude of possible interactions between ligand and metal-centered orbitals. We consider here only the ligand orbitals which are relevant for the lowest energy LMCT transitions, since these are the observed ones. LMCT transitions involving ligand orbitals with σ symmetry with respect to the Cr−O axis occur at higher energies than those involving orbitals with π symmetry.[13] Therefore only ligand orbitals which have π symmetry with respect to both Cr−O bonds are considered. These all lie in the plane defined by the three bridging oxygens (see Figure 7), and they transform as a_2 and e in the approximate C_{3v} single-ion frame. The only symmetry-allowed metal−ligand interaction is thus of e type, and the corresponding one-electron transfer integral is defined as

$$h_{\pi_{ML}} = \langle (e_x)_A | \hat{h} | (e_x)_L \rangle = \langle (e_x)_L | \hat{h} | (e_x)_B \rangle = \langle (e_y)_A | \hat{h} | (e_y)_L \rangle = \langle (e_y)_L | \hat{h} | (e_y)_B \rangle \qquad (4)$$

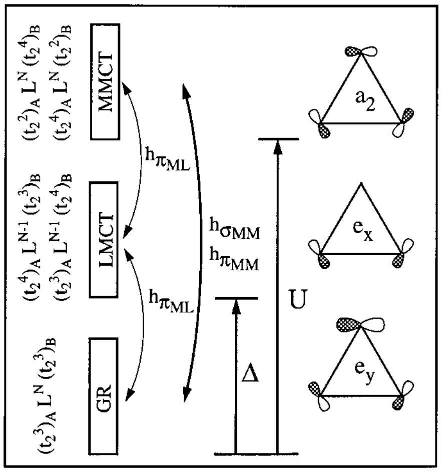

Figure 7. Vizualization of the model parameters described in the text. The ground, LMCT, and MMCT electron configurations are schematically shown on the left. The ligand orbitals lying in the plane formed by the three oxygen atoms are shown on the right.

Scheme 2

	GR	LMCT	MMCT
GR	δ_{t_2} $R(^2E)$ $R(^2T_1)$ $R(^2T_2)$	$h_{\pi_{ML}}$	$h_{\sigma_{MM}}$ $h_{\pi_{MM}}$
LMCT	$h_{\pi_{ML}}$	B Δ $h_{\sigma_{MM}}$ C δ_{t_2} $h_{\pi_{MM}}$	$h_{\pi_{ML}}$
MMCT	$h_{\sigma_{MM}}$ $h_{\pi_{MM}}$	$h_{\pi_{ML}}$	B U C δ_{t_2}

A total of 834 pair functions comprising all three electron configurations in eq 1 are used for the calculation. They were generated as linear combinations of Slater determinants similar to those reported in ref 16 using Clebsch−Gordon and point group coupling coefficients.[17] The structure of the resulting energy matrix is shown in Scheme 2.

The state splittings of the CT configurations are parametrized by the Racah parameters B and C, which are connected to the $R(^2E)$ parameter by $C = 4B$ and $21B = R(^2E)$. The exchange interactions arise from the mixing induced by the parameters $h_{\sigma_{MM}}$, $h_{\pi_{MM}}$, $h_{\pi_{ML}}$ in the off-diagonal blocks of Scheme 2. The energy matrix was set up in a basis of all 834 functions and diagonalized numerically with some fixed and some adjustable parameters as discussed in section 5.2.

4.2. Exchange Parameters. Exchange splittings in the ground state are often described in terms of the isotropic Heisenberg Hamiltonian

$$H = J_{GS} \mathbf{S_A} \cdot \mathbf{S_B} \qquad (5)$$

where a positive value for J_{GS} corresponds to an antiferromagnetic splitting. This gives rise to the well-known Landé

---

(16) Glerup, J. *Acta Chem. Scand.* **1972**, *26*, 3775.

(17) Rotenberg, M.; Bivis, R.; Metropolis, N.; Wooten, J. K., Jr. *The 3-j and 6-j Symbols*; The Technology Press: Cambridge, MA, 1959.

splitting pattern characterized by

$$E(S) - E(S-1) = J_{GS}S \qquad (6)$$

In terms of our model the parameter J_{GS} is given by a sum of orbital exchange parameters as follows:

$$J_{GS,model} = (1/9)(J_a + 2J_e) \qquad (7)$$

where J_a and J_e represent the exchange pathways involving the a_1 (eq 2) and e (eqs 3 and 4) metal-centered orbitals. J_a and J_e can be expressed in terms of the model parameters in section 4.1 as follows:[18]

$$J_a = 4\left(\frac{h_{\sigma_{MM}}^{\;2}}{U}\right) \qquad (8)$$

$$J_e = 4\left[\left(\frac{h_{\pi_{MM}}^{\;2}}{U}\right) + \left(\frac{h_{\pi_{ML}}^{\;2}}{\Delta}\right)^2\left(\frac{1}{U} + \frac{1}{\Delta}\right)\right] \qquad (9)$$

Equations 8 and 9 represent a rather crude approximation, because the expansions are only taken to second order for $h_{\sigma_{MM}}$ and $h_{\pi_{MM}}$ and to fourth order for $h_{\pi_{ML}}$.

5. Analysis

5.1. Intensity Mechanisms. There are two well-established intensity-giving mechanisms for dimer transitions which are spin-forbidden in the single ion:[19] (i) a single-ion mechanism which is due to the combined action of the odd-parity ligand field at the single-ion site and spin−orbit coupling; (ii) an electric-dipole exchange mechanism. The latter, which was first proposed by Tanabe and co-workers,[20,21] turned out to be the most effective intensity-providing mechanism for pair transitions within the t_2 orbitals (in O notation). For a general pair transition involving orbital changes $A(i \rightarrow k)$ and $B(j \rightarrow l)$ in a dimer, the interaction of the electric vector $\vec{E}$ of the incident light with the electric-dipole transition moment can be expressed as

$$H = \sum_{i,j,k,l} (\vec{\Pi}_{A_{i,k}B_{j,l}} \cdot \vec{E})(\vec{s}_{A_{i,k}} \cdot \vec{s}_{B_{j,l}}) \qquad (10)$$

where $A_{i,k}$ and $B_{j,l}$ represent the singly occupied orbitals a_1 and e on the two metal centers, and $\vec{s}_{A_{i,k}}$, $\vec{s}_{B_{j,l}}$ are one-electron spin operators.[21,22] The Hamiltonian H has to be invariant under the symmetry operations of the dimer point group, and $\Delta S = 0$ has to be fulfilled. For the title complex with D_{3h} symmetry the electric-dipole selection rules are as follows:

$$\begin{aligned} &{}^1A_1' \xrightarrow{\sigma} {}^1E' \qquad {}^1A_1' \xrightarrow{\pi} {}^1A_2'' \\ &{}^3A_2'' \xrightarrow{\sigma} {}^3E'' \qquad {}^3A_2'' \xrightarrow{\pi} {}^3A_1' \\ &{}^5A_1' \xrightarrow{\sigma} {}^5E' \qquad {}^5A_1' \xrightarrow{\pi} {}^5A_2'' \end{aligned} \qquad (11)$$

An important consequence of eq 11 is that in π polarization all the symmetric DE where the electrons are equally distributed over the orbitals on both centers are prohibited. This is the case for $^2E^2E$, $^2E(^2T_1)^2E(^2T_1)$, and $^2A_2(^2T_1)^2A_2(^2T_1)$; see Table 3. On the other hand, DE to $^2A_2{}^2A_2$ and $^2A_2{}^2A_1$ are prohibited in σ polarization, since these states are invariant under $\hat{C}_3$.

Table 3. Symmetry Labels of the Terms of the $^2E^2E$, $^2E^2T_1$, $^2T_1{}^2T_1$, $^2E^2T_2$, and $^2T_1{}^2T_2$ DE States[a]

O	C_{3v}	D_{3h}
$^2E^2E$		$^3A_2''\ ^1A_1'\ ^3A_2'\ ^1A_1''\ ^3E''\ ^1E'$
$^2E^2T_1$	$^2E^2E$	$^3A_2''\ ^1A_2''\ ^3A_1''\ ^1A_1''\ ^3E''\ ^1E''$ $^3A_1'\ ^1A_1'\ ^3A_2'\ ^1A_2'\ ^3E'\ ^1E'$
	$^2E^2A_2$	$^3E''\ ^1E''\ ^3E'\ ^1E'$
$^2T_1{}^2T_1$	$^2A_2{}^2A_2$	$^3A_2''\ ^1A_1'$
	$^2E^2A_1 \pm {}^2E^2A_1$	$^3E''\ ^1E''\ ^3E'\ ^1E'$
	$^2E^2E$	$^3A_2''\ ^1A_1'\ ^3A_2'\ ^1A_1''\ ^3E''\ ^1E'$
$^2E^2T_2$	$^2E^2E$	$^3A_2''\ ^1A_2''\ ^3A_1''\ ^1A_1''\ ^3E''\ ^1E''$ $^3A_1'\ ^1A_1'\ ^3A_2'\ ^1A_2'\ ^3E'\ ^1E'$
	$^2E^2A_1$	$^3E''\ ^1E''\ ^3E'\ ^1E'$
$^2T_1{}^2T_2$	$^2A_2{}^2A_1$	$^3A_1''\ ^1A_1''\ ^3A_2'\ ^1A_2'$
	$^2A_2{}^2E$	$^3E''\ ^1E''\ ^3E'\ ^1E'$
	$^2E^2A_1$	$^3E''\ ^1E''\ ^3E'\ ^1E'$
	$^2E^2E$	$^3A_2''\ ^1A_2''\ ^3A_1''\ ^1A_1''\ ^3E''\ ^1E''$ $^3A_1'\ ^1A_1'\ ^3A_2'\ ^1A_2'\ ^3E'\ ^1E'$

[a] The representations in the single-ion point groups O and C_{3v} are listed on the left. The arising terms in the approximate D_{3h} dimer symmetry are shown on the right.

Table 4. Vibronic Selection Rules for Dimer Excitations in D_{3h} Symmetry Using the Enabling Modes Transforming as a_2'', e', and e''

		excited level, polarizn	
mode	ground level	σ	π
a_2''	$^1A_1'$	$^1E''$	$^1A_1'$
	$^3A_2''$	$^3E'$	$^3A_2''$
e'	$^1A_1'$	$^1A_1'\ ^1A_2'\ ^1E'$	$^1E''$
	$^3A_2''$	$^3A_2''\ ^3A_1''\ ^3E''$	$^3E'$
e''	$^1A_1'$	$^1A_1''\ ^1A_2''\ ^1E''$	$^1E'$
	$^3A_2''$	$^3A_1'\ ^3A_2'\ ^3E'$	$^3E''$

A third intensity mechanism is that induced by vibronic coupling to enabling modes. Forbidden transitions can be made allowed and the intensity of allowed transitions can be enhanced by this mechanism.[23] In the basic rhodo complex, $[(NH_3)_5CrOCr(NH_3)_5)]^{4+}$,[22] and in $KMgF_3{:}Mn^{2+}$ [24] it was found that a vibronically induced electric-dipole exchange mechanism is very efficient in providing intensity to DE, particularly those which are forbidden in the normal electric-dipole mechanism. Vibrations involving the bridging oxygen atoms are expected to be most important in providing vibronic intensity, since they directly influence the geometry of the CrO_3Cr central core. In the limit of no coupling between bridging and terminal motions, only the nine metal−ligand vibrational degrees of freedom of the CrO_3Cr core contribute to vibrations involving the oxygen atoms. A normal coordinate analysis of the isostructural complex $[Fe_2(OH)_3(tmtacn)_2]^{2+}$ revealed that these internal core coordinates combine to generate two a_1' (316 and 124 cm^{-1}), one a_2'' (306 cm^{-1}), two e' (188 and 97 cm^{-1}), and one e'' (230 cm^{-1}) normal modes of vibration in D_{3h} symmetry.[25] The energies are assumed to be only slightly modified in **1** compared to $[Fe_2(OH)_3(tmtacn)_2]^{2+}$, and we are therefore using these values. Considering the latter three modes, we derive the vibronic selection rules shown in Table 4 for the relevant dimer excitations.

In sections 5.2 and 5.3 the observed SE and DE bands will be analyzed in detail by considering the above intensity

---

(18) Weihe, H.; Toftlund, H.; Güdel, H. U. Submitted to *Inorg. Chem.*
(19) Naito, M. *J. Phys. Soc. Jpn* **1973**, *34*, 1491.
(20) Gondaira, K. I.; Tanabe, Y. *J. Phys. Soc. Jpn*. **1966**, *21*, 1527.
(21) Ferguson, J.; Guggenheim, H. J.; Tanabe, Y. *J. Phys. Soc. Jpn.* **1966**, *21*, 692.
(22) Güdel, H. U.; Dubicki, L. *Chem. Phys.* **1974**, *6*, 272.
(23) Herzberg, G. *Electronic Spectra of Polyatomic Molecules*; Van Nostrand Reinhold Company: New York, NY, 1966.
(24) Güdel, H. U. *Chem. Phys. Lett.* **1975**, *36*, 328.
(25) Gamelin, D. R.; Bominaar, E. L.; Mathonière, C.; Kirk, M. L.; Girerd, J.-J.; Wieghardt, K.; Solomon, E. I. *Inorg. Chem.* **1996**, *35*, 4323.

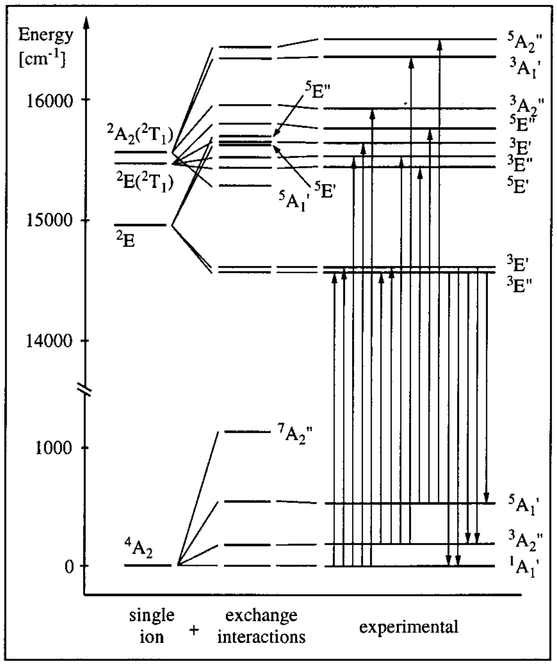

Figure 8. Energy level diagram of the $^2E^4A_2$, $^2T_1{}^4A_2$ singly excited states. On the left the single-ion energy levels in the absence of exchange interactions are shown. In the middle row the interactions represented by the one-electron parameters $h_{\sigma_{MM}}$, $h_{\pi_{MM}}$, and $h_{\pi_{ML}}$ are introduced. On the right the experimental values are shown. The dimer levels are labeled in the approximate D_{3h} symmetry.

mechanisms. The overview absorption spectra in Figure 1 show that in the whole region of d−d bands the π:σ intensity ratio is roughly 3:1. For the DE this predominance of π intensity is explained as follows. As will be demonstrated in section 5.5, the dominant configurational mixing of DE dimer levels under the action of $\hat{h}$ occurs with the MMCT configuration. This mixing is not only responsible for the energy splittings of the dimer levels, but also for the intensity of the DE through the $\vec{\Pi}_{A_{i,k}B_{j,l}}$ coefficients in eq 10. MMCT excitations are necessarily π polarized, and this explains the $\pi > \sigma$ intensity in the DE region. For the spin-allowed d-d transitions $^4A_2 \rightarrow {}^4T_2$ and $^4A_2 \rightarrow {}^4T_1$, one usually considers LMCT excitations as the principal source of intensity. It can be shown that this mixing cannot take place with the lowest energy LMCT bands observed in the spectrum. We therefore have no direct experimental evidence for a π dominance in the relevant LMCT excitations at higher energy. However, at these high energies above 50 000 cm^{-1} there is substantial CI between the LMCT and MMCT configurations which will induce a dominance of π intensity.

5.2. Single Excitations. The absorption spectra in the region of the $^4A_2{}^4A_2 \rightarrow {}^2E^4A_2$, $^2T_1{}^4A_2$ SE bands as well as the luminescence spectrum are similar to the corresponding spectra of **2** reported in ref 7. This allows an assignment in complete analogy; the results are given in Table 1 and Figure 8. In the ground state the dimer spin ranges from $S = 0$ to $S = 3$, whereas in the SE states $S^* = 1, 2$. Since at 10 K only the $S = 0$ ground state level is populated, all the cold bands in the absorption spectrum are spin-forbidden and thus gain their intensity by the single-ion mechanism. As a consequence, also the orbital selection rules are relaxed for the cold transitions. On the other hand, the hot bands may have intensity from both the single-ion and exchange mechanisms. A number of hot bands are typically 1−2 orders of magnitude more intense than the corresponding cold bands (see Table 1), indicating an exchange mechanism. The weak, sharp lines on the high-energy side of the $^4T_2$ band (see Figure 1) are assigned to $^2T_2{}^4A_2$ SE, but due to the poor resolution of these bands an assignment to distinct dimer transitions is not possible.

5.3. Double Excitations. In Table 3 all the dimer levels (in D_{3h}) arising from the $^2E^2E$, $^2E^2T_1$, $^2T_1{}^2T_1$, $^2E^2T_2$, and $^2T_1{}^2T_2$ DE states are summarized. According to the selection rules (eq 11), there are only 3 and 10 allowed cold transitions in π and σ polarization, respectively. Experimentally, 28 π and 27 σ polarized cold bands are observed in the DE region; see Table 2. This is an indication that some DE are induced by a vibronic intensity-gaining mechanism. Applying the vibronic selection rules in Table 4 to the DE in Table 3 yields 32 and 61 vibronically allowed cold transitions in π and σ polarization, respectively. We conclude that part of the intensity in the DE region is vibronic. This is supported by the fact that the relative intensities of the DE bands span a range of 3 orders of magnitude; see Table 2. In contrast, the configurational mixing coefficients between the DE and MMCT configurations, which are mainly responsible for the DE intensities (see section 5.1), vary within 1 order of magnitude. This strongly suggests a vibronic intensity mechanism which selectively amplifies the intensity of some DE bands.

The complexity of the spectra prohibits a complete assignment of all the observed individual bands. However, the most prominent ones can be assigned by analogy to the basic rhodo complex. In this dimer the intensity in the DE region is exclusively π polarized, and it is induced by vibronic coupling of the antisymmetric Cr−O−Cr stretching mode to symmetric DE.[22] This is highly efficient due to the strong superexchange pathway along the z axis. In the title complex the situation is similar in that the dominant exchange pathway is also the direct one along z (see section 6.2). We thus assign the five intense cold π polarized bands at 28 297, 29 875, 30 876, 33 422, and 37 600 cm^{-1} to $^1A_1' \rightarrow {}^1A_1' \otimes a_2''$ vibronic transitions. Similarly, the intense hot bands at 29 400 and 31 130 cm^{-1} are assigned to $^3A_2'' \rightarrow {}^3A_2'' \otimes a_2''$ transitions. The assignment is summarized in Table 2.

In σ polarization the situation is less clear. In the normal coordinate analysis on $[Fe_2(OH)_3(tmtacn)_2]^{2+}$ it was found that the electric-dipole moment perpendicular to z induced by the 97 cm^{-1} e′ mode is much larger than that by the e″ mode.[25] We tentatively assign the three most prominent σ bands at 29 124 cm^{-1} (hot), 29 600 cm^{-1} (cold), and 34 482 cm^{-1} (cold) to the transitions $^3A_2'' \rightarrow {}^3A_2''$ $(^2A_2{}^2A_2) \otimes e'$, $^1A_1' \rightarrow {}^1A_1'$ $(^2A_2{}^2A_2) \otimes e'$, and $^1A_1' \rightarrow {}^1A_2'$ $(^2A_2{}^2A_1) \otimes e'$, respectively. Note that both bands at 29 600 cm^{-1} (σ) and 29 875 cm^{-1} (π) are vibronic bands built on the same electronic origin. Similarly with the hot bands at 29 124 cm^{-1} (σ) and 29 400 cm^{-1} (π). Their energy difference of 275 cm^{-1} is in reasonable agreement with the energy difference between the lower e′ mode (97 cm^{-1}) and the a_2'' mode (306 cm^{-1}) in the $[Fe_2(OH)_3(tmtacn)_2]^{2+}$ complex.

5.4. LMCT Transitions. In the absorption spectra shown in Figures 4 and 6 three LMCT bands are observed at 34 000, 40 600, and 41 200 cm^{-1}, labeled by I, II, and III, respectively. Band I is hot and completely σ polarized. It is thus assigned to a $^3A_2'' \rightarrow {}^3E''$ transition in D_{3h} notation. Similarly, the π-polarized cold band II is assigned to a $^1A_1' \rightarrow {}^1A_2''$ LMCT transition. The weak π-polarized cold band III is assigned to $^1A_1' \rightarrow {}^1A_1''$, which is symmetry-forbidden in the approximate symmetry D_{3h}, but becomes allowed in the actual C_{3h} symmetry.[14] The $^3E''$ level is thus the lowest LMCT level, clearly indicating a ferromagnetic energy ordering of the lowest-energy LMCT levels.

Table 5. Comparison of Parameter Values Obtained for $[Cr_2(OH)_3(tmtame)_2](NO_3)_3$ (**1**) and $[Cr_2(OH)_3(tmtacn)_2](ClO_4)_3$ (**2**)[a]

	1	2		1	2
U	90000	90000	$h_{\pi_{MM}}$	−2366	−1261
Δ	39000	39000	$h_{\pi_{ML}}$	−3905	−2011
$R(^2T_2)$	21000	21000	J_{GS}	175	136
$R(^2T_1)$	15536	15608	$J_{GS,model}$	222	146
$R(^2E)$	14947	14713	J_a	1456	1171
δ_{t_2}	701	1622	J_e	271	72
$h_{\sigma_{MM}}$	−5723	−5132	J_a/J_e	5.4	16.3

[a] The model parameters obtained from the energy fits are shown on the left, the exchange parameters on the right. J_{GS} is the experimental exchange parameter for the ground state (all values in cm^{-1} expect of J_a/J_e).

5.5. Energy Calculations. The model parameters were determined as follows. The MMCT energy U cannot be directly derived from experiment. The upper limit of 146 000 cm^{-1} obtained from the free-ion ionization potentials[26] is assumed to be lowered to about 50−60% in solids.[9] We set U to 90 000 cm^{-1}, as estimated in ref 27. Δ was set to 39000 cm^{-1}, which lies roughly 2000 cm^{-1} above the center of gravity of the LMCT bands I and II. The single-ion energy $R(^2T_2)$ was fixed at 21 000 cm^{-1}, within the range of the observed $^4A_2{}^4A_2 \rightarrow {}^2T_2{}^4A_2$ transitions; see Figure 1.

The trigonal splitting δ_{t_2}, the single-ion energies $R(^2E)$ and $R(^2T_1)$, and the transfer integrals $h_{\sigma_{MM}}$, $h_{\pi_{MM}}$, and $h_{\pi_{ML}}$ were determined by a least-squares fit to the 13 observed transitions between the $^4A_2{}^4A_2$ ground and the $^2E^4A_2$ and $^2T_1{}^4A_2$ SE levels (see Table 1) as well as the LMCT bands II and III. The ground state splitting is thus included in the fit of 6 parameters to 15 observations. The value $\delta_{t_2} = 701$ cm^{-1} thus obtained is in good agreement with the value of 670 cm^{-1} calculated independently from the observed trigonal splitting of the $^4T_2$ and $^4T_1$ ligand field states. The single-ion energies $R(^2E) = 14\,947$ cm^{-1} and $R(^2T_1) = 15\,536$ cm^{-1} lie within the range of the observed $^2E^4A_2$ and $^2T_1{}^4A_2$ SE, respectively; see Figure 2 and Table 1.

The three electron-transfer parameters $h_{\sigma_{MM}} = -5723$ cm^{-1}, $h_{\pi_{MM}} = -2366$ cm^{-1}, and $h_{\pi_{ML}} = -3905$ cm^{-1} are all negative, indicating that the overlap between the corresponding orbitals is positive, as derived from Hückel theory. The value for $h_{\sigma_{MM}}$ is in excellent agreement with $|h_{\sigma_{MM}}| = 5516-6538$ cm^{-1} reported for the mixed-valence system $[Fe_2(OH)_3(tmtacn)_2]^{2+}$.[28] A value $|h_{\pi_{ML}}| \approx 10\,000$ cm^{-1} was estimated for an oxide ligand.[13] For the hydroxide ligands in **1** this will be significantly reduced due to the increase in the Cr−O distance from ≈ 1.80 to 1.97 Å as well as the presence of the protons.

We have also applied our model on **2**. U, Δ, and $R(^2T_2)$ were fixed at the same values as for **1**. The remaining parameters were obtained by a least-squares fit to 10 observed $^4A_2{}^4A_2 \rightarrow {}^2E^4A_2$, $^2T_1{}^4A_2$ transitions reported in ref 7. The parameter values for both complexes **1** and **2** are summarized in Table 5. All the transfer integrals are lower by up to 50% in **2** compared to **1**. The trigonal field parameter $\delta_{t_2} = 1622$ cm^{-1} for **2** is more than twice as large as for **1** and corresponds to a value of $\delta_{t_2} = 1000$ cm^{-1} obtained from a complete ligand-field calculation.[29]

The energy levels are obtained from diagonalization of the energy matrix with the model parameter values presented in Table 5. Figure 8 shows the energy diagram of the $^4A_2{}^4A_2$ ground and $^2E^4A_2$, $^2T_1{}^4A_2$ SE states for **1**. On the left the situation is shown for the two monomeric constituents of the complex in C_{3v} symmetry, in the absence of any exchange interaction. The $^2T_1{}^4A_2$ state is split due to the trigonal field. Under the influence of the interactions represented by the transfer integrals $h_{\sigma_{MM}}$, $h_{\pi_{MM}}$, and $h_{\pi_{ML}}$, the splitting pattern shown in the middle part of Figure 8 is obtained. On the right the experimental scheme is shown. The agreement between calculated and observed energy levels is excellent.

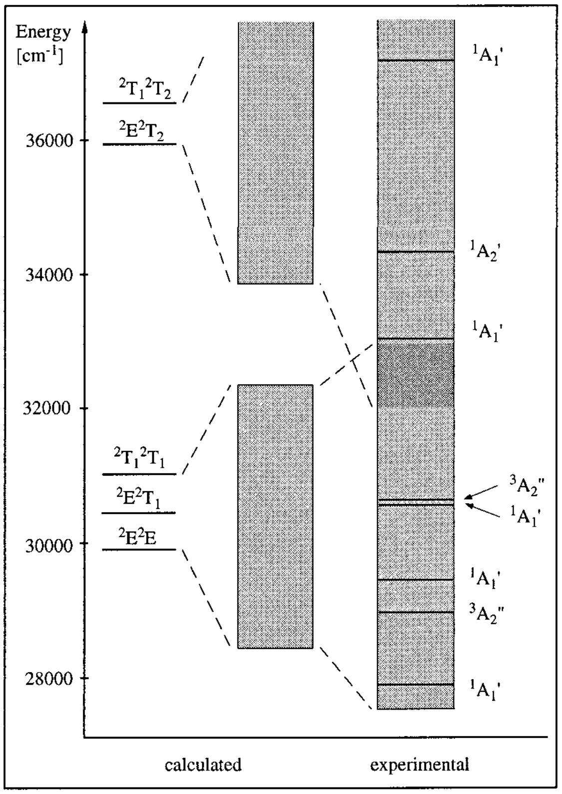

Figure 9. Energy level diagram in the DE region. On the left the single-ion energy levels are shown. In the middle the trigonal field δ_{t_2} as well as the interactions represented by the one-electron parameters $h_{\sigma_{MM}}$, $h_{\pi_{MM}}$, and $h_{\pi_{ML}}$ are introduced. On the right the experimental values are shown. The terms are labeled in the approximate D_{3h} symmetry. The shadowed areas represent the total energy spread.

Figure 9 shows the energy diagram of the DE. The shadowed areas represent the total spreads of dimer levels originating from the corresponding single-ion states on the left of Figure 9. On the right the experimental situation is shown, and observed electronic energy levels of vibronic bands assigned in section 5.3 are shown. From a comparison with **2** reported in ref 7, we assume the overlap region between the lower DE, $^2E^2E$, $^2E^2T_1$, $^2T_1{}^2T_1$, and the higher ones, $^2E^2T_2$, and $^2T_1{}^2T_2$, to lie between 32 000 and 33 000 cm^{-1}, represented by the dark-shaded area at the right-hand side of Figure 9. For the $^2E^2E$, $^2E^2T_1$, $^2T_1{}^2T_1$ DE the bulk of calculated energy levels lies about 1000 cm^{-1} too high in energy compared to experiment, and the total splitting is about 25% too small. The same appears to be true for the higher $^2E^2T_2$, and $^2T_1{}^2T_2$ DE.

6. Discussion

6.1. The Model. As shown in section 5.5, the agreement between observed and calculated energy splittings is excellent for the ground and SE states (see Figure 8), whereas for the DE states the splittings obtained from the model are too small by about 25% (see Figure 9). The exchange interactions in the

---

(26) *Handbook of Chemistry and Physics*; CRC Press: Boca Raton FL, 1988−1989; table with ionization potentials.

(27) Atanasov, M.; Angelov, S. *Chem. Phys.* **1991**, *150*, 383.

(28) Gamelin, D. R.; Bominaar, E. L.; Kirk, M. L.; Wieghardt, K.; Solomon, E. I. *J. Am. Chem. Soc.* **1996**, *118*, 8085.

(29) Riesen, H. Dissertation, Universität Bern, 1987.

latter are thus underestimated by the model. We ascribe these differences mainly to the fact that only two ligand orbitals are included in the model. Inclusion of additional ligand orbitals would result in a multitude of higher energy LMCT transitions, whose presence would become more evident in the DE compared to the SE states. Of minor importance is the fact that no transitions to DE states were included in the least-squares fit of calculated energies. Inclusion of the assigned DE levels in Table 2 and Figure 9 would be ambiguous and turned out to be impractical.

Translation of our model parameters to the exchange parameters J_a, J_e, and $J_{GS,model}$ using eqs 7−9 (see Table 5) reveals the following. $J_{GS,model}$ is calculated 26% higher than J_{GS} for **1**, and is thus a direct result of the approximate character of eqs 8 and 9 and thus eq 7. We note, however, that the observed ground-state splitting is very well reproduced by the full diagonalization of the energy matrix: a singlet−triplet splitting of 173 versus 175 cm^{-1} experimentally. The approximation is therefore not in the model itself, but in the translations (8) and (9). The value of these equations lies in the fact that they visualize what happens when we go from the ground state to the SE or DE states: The denominators U and Δ are reduced by roughly 15 000 and 30 000 cm^{-1}, respectively, leading to significant increases of J_a and J_e. In earlier treatments, e.g., in the analysis of the observed exchange splittings in complex **2**, the splittings in the ground and SE states had been modeled separately, and significantly higher J values had been observed for the SE states.[7] In the model presented here this increase is automatically incorporated.

6.2. Exchange Pathways and Comparison between 1 and 2. The relative importance of the different exchange pathways represented by $h_{\sigma_{MM}}$, $h_{\pi_{MM}}$, and $h_{\pi_{ML}}$ can be seen from eqs 8 and 9. The dimer levels of the ground configuration do not split upon mixing with those of the LMCT configuration unless the latter themselves mix with MMCT dimer levels.[9−12,18] The interaction between the ground and LMCT configurations is thus of higher order than that between the ground and MMCT configurations; see eqs 8 and 9. Insertion of the model parameters in Table 5 into eq 9 reveals that the contribution of $h_{\pi_{ML}}$ to J_e, i.e., the superexchange, is only on the order of about 5%. The direct exchange pathway along the Cr−Cr axis is dominant, and the σ contribution exceeds the π contribution by about 1 order of magnitude. This situation is consistent with the results of earlier studies on $[Cr_2(OH)_3(tmtacn)_2](ClO_4)_3$,[7] $Cs_3Cr_2Cl_9$,[30] and V^{2+} pairs in $CsMg_{1-x}V_xCl_3$.[31] As a consequence of the short Cr−Cr distance, there is a substantial σ overlap of the a_1 metal-centered orbitals. On the other hand, the direct π overlap of the e metal-centered orbitals is much smaller.

The values of $h_{\sigma_{MM}}$, $h_{\pi_{MM}}$, and $h_{\pi_{ML}}$ in Table 5 show that the interaction along all the pathways is larger in **1** than in **2**. For the direct pathways this can be correlated to the different Cr−Cr separations of 2.636[15] and 2.664 Å,[7] respectively, in terms of the resulting change of direct overlap of the metal-centered orbitals. In the case of the e orbitals, the direct overlap represented by $h_{\pi_{MM}}$ increases by about a factor of 2 for **1** compared to **2**, whereas for the a_1 orbitals the increase of $h_{\sigma_{MM}}$ is only about 12%. This demonstrates that the smaller the overlap, the larger the relative change upon changing the Cr−Cr distance. Using eqs 7−9 the change of the transfer integrals can be expressed in changes of the exchange parameters. The rise of J_a by 24% in **1** compared to **2** is thus directly correlated to the decrease of 0.03 Å in Cr−Cr separation. Similarly, J_{GS} is increased by 30%. This is in excellent agreement with the results from experiments on **2** under hydrostatic pressure,[32] revealing that a shortening of only 0.01 Å in the Cr−Cr separation results in a 10% increase of J_a and J_{GS}.

The trigonal field parameter δ_{t_2} is increased from 701 to 1622 cm^{-1} for **2** compared to **1**; see Table 5. This enhancement can be explained with structural differences imposed by the terminal ligands. In $[Cr_2(OH)_3(tmtame)_2](NO_3)_3$ the methyl groups on the nitrogen atoms of the tmtame ligands are slightly rotated around the trigonal axis. In $[Cr_2(OH)_3(tmtacn)_2](ClO_4)_3$ they are eclipsed, giving rise to a sterically unfavorable situation, leading to an increase of the Cr−Cr and Cr−O distances and thus an increase of the trigonal field.

The observed ferromagnetic energy ordering of the lowest LMCT levels is also the result of the dominant direct exchange pathways. With reference to ref 14 this behavior is explained as follows. The metal part of the LMCT configurations $(t_2^4)_A L^{N-1}(t_2^3)_B/(t_2^3)_A L^{N-1}(t_2^4)_B$ is exactly analogous to the ground electron configuration of mixed-valence systems. The result is a spin-dependent electron transfer between the metal centers and an exchange phenomenon called double exchange.[33] The transferred electron can be restored in either the a_1 or e orbital on the accepting metal. As shown in Scheme 2, the interaction between the two LMCT configurations $(t_2^4)_A L^{N-1}(t_2^3)_B/(t_2^3)_A L^{N-1}(t_2^4)_B$ is determined by the matrix elements $h_{\sigma_{MM}}$ and $h_{\pi_{MM}}$ for the a_1 and e metal-centered orbitals, respectively; see eqs 2 and 3. The resulting total splitting of the lowest-energy LMCT levels is equal to twice the value of $h_{\sigma_{MM}}$, and the energy ordering in the lower sets of levels is ferromagnetic. The superexchange interaction parametrized by $h_{\pi_{ML}}$ was found to give only a minor antiferromagnetic contribution to the energy ordering of LMCT levels, which is thus reversed compared to the ground state. This behavior can be expected whenever there is an efficient direct exchange pathway in a coupled system.

In conclusion, the VBCI model developed to account for exchange splittings in the LMCT configurations of Cu^{2+} and Fe^{3+} dimers was adapted to the specific situation in **1** and **2** and successfully extended for the description of the ground, SE, and DE states. The observed energy splittings are well reproduced over an energy range of over 40 000 cm^{-1}. From the model parameters orbital exchange parameters can be derived, revealing the relative efficiencies of different exchange pathways. We want to stress that this global model only requires one set of parameters. This is in contrast to all previous treatments in which the exchange splittings in the various states were modeled separately. The well-known increase of exchange interactions with energy is nicely reproduced by our model, demonstrating the important role of electron-transfer processes as a main source of exchange interactions.

Acknowledgment. Financial support from the Swiss National and European Science Foundations is gratefully acknowledged.

IC9904081

---

(30) Leuenberger, B.; Güdel, H. U. *Inorg. Chem.* **1986**, *25*, 181.
(31) Riesen, H.; Güdel, H. U. *Inorg. Chem.* **1984**, *23*, 1880.
(32) Riesen, H.; Güdel, H. U. *J. Chem. Phys.* **1987**, *87*, 3166.
(33) Blondin, G.; Girerd, J.-J. *Chem. Rev.* **1990**, *90*, 1359.